

Colloidal spray pyrolysis: A new fabrication technology for nanostructured energy storage materials



Yujia Liang^a, Huajun Tian^{a,b,*}, Joseph Repac^a, Sz-Chian Liou^c, Ji Chen^a, Weiqiang Han^{b,e}, Chunsheng Wang^{a,*}, Sheryl Ehrman^{a,d,*}

^a Department of Chemical and Biomolecular Engineering, University of Maryland, College Park, MD 20742, USA

^b Ningbo Institute of Materials Technology and Engineering, Chinese Academy of Sciences, Ningbo 315201, China

^c AIM Lab, NanoCenter, University of Maryland, College Park, MD 20742, USA

^d Charles W. Davidson College of Engineering, San Jose State University, San Jose, CA 95192, USA

^e School of Materials Science and Engineering, Zhejiang University, Hangzhou 310027, China

ARTICLE INFO

Keywords:

Colloidal spray pyrolysis
Process development
Solid-state reactions
Lithium-ion and sodium-ion batteries
EELS

ABSTRACT

Spray pyrolysis is a scalable process to fabricate functional particles as cathode/anode materials in rechargeable batteries from precursor solutions. However, one prerequisite of spray pyrolysis to achieve uniform particle-to-particle composition and structure is a stable precursor solution, restricting its usage to highly soluble salts. Otherwise, extremely acidic precursors are necessary to ease the uncontrollable hydrolysis of the salts and the subsequent precipitation. Moreover, strong reducing agents such as H₂ are also needed for complete solid-state reactions, introducing potential safety concerns. Herein, for the first time, we develop a novel process, colloidal spray pyrolysis (CSP), which can eliminate all the prerequisites simultaneously. Our process can generate particles directly from a multiphase precursor in mild processing conditions through *in-situ* solid-state reactions. The product structure and composition can be precisely designed based on aerosol dynamics and reaction kinetics. By applying CSP, Sn@C particles with three distinct interior nanostructures have been synthesized and evaluated as anodes for lithium-ion batteries (LIBs) and sodium-ion batteries (SIBs). The best performing Sn@C anode delivers 627.9 mAh/g at 2 C with capacity retention of 88.5% after 1500 cycles in LIBs and demonstrates superior rate capability for SIBs. This novel CSP process is promising in preparing electrode materials in LIBs and SIBs for future practical applications.

1. Introduction

Spray pyrolysis is a scalable process with low operating cost, high process throughput, and minimal waste production [1–3]. It has been widely used to fabricate functional particles for many applications, including catalysts [4], lithium-ion batteries (LIBs) and sodium-ion batteries (SIBs) [5,6], and superconductors [7]. A stable precursor solution with all salts dissolved is a necessity, or the precipitation in the precursor solution during spray pyrolysis can lead to product particles with non-uniform particle-to-particle composition and structure [8]. Therefore, it is challenging to synthesize functional particles from aqueous solutions containing poorly-soluble or easily-hydrolyzed salts. To resist precipitation, metal salts with strong acids and pure organic solvents are normally used to form stable precursor solutions (Route (I), Fig. 1) [9,10]. H₂ is typically introduced into the carrier gas to promote the complete reduction of the salts [9], or residual oxides could be formed in the products [11,12]. However, potential safety

concerns accompanied with the use of low flash point organic solvents (*e.g.*, ethanol, 13 °C), an acidic precursor, and explosive gas (H₂) make industrial-scale production difficult [13,14].

Here, we present colloidal spray pyrolysis (CSP) for the first time, a process that can generate functional particles with uniform particle-to-particle composition and structure from stable multiphase precursor solutions (Route (II), Fig. 1), which could be a promising strategy to prepare uniform electrode materials in LIBs and SIBs. The structure and composition of particles are pre-designable based on our models. Several distinguishable advantages of CSP make it unique when compared to conventional aerosol processes. Unlike spray pyrolysis, CSP can process low solubility salts, expanding the application of spray pyrolysis to a wider range of functional materials. CSP uses an aqueous precursor solution, with no direct addition of H₂ gas or pure organic solvents, which makes CSP safer and simpler for scale-up manufacturing. CSP is also different from multi-step spray drying, where colloids are used as templates to be etched away in the end [15,16]. CSP is a

* Corresponding authors.

E-mail addresses: tianhuajun@nimte.ac.cn (H. Tian), cswang@umd.edu (C. Wang), sehrman@umd.edu (S. Ehrman).

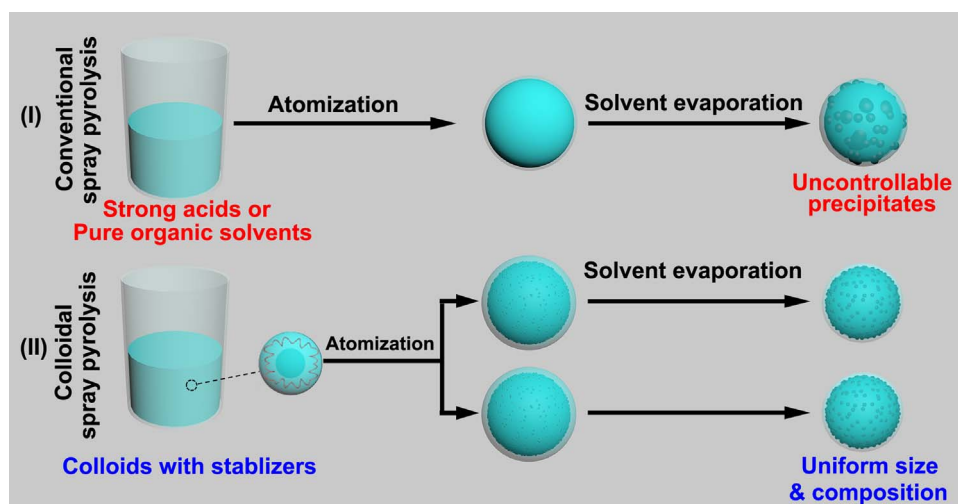


Fig. 1. A comparison of conventional spray pyrolysis (Route I) and colloidal spray pyrolysis (Route II).

one-step process with a short residence time where colloids are involved in *in-situ* solid-state reactions and structural evolution.

To evaluate the robustness of CSP, we targeted tin@carbon (Sn@C) nanocomposite particles that are difficult to synthesize by conventional spray pyrolysis because Sn salts are easily hydrolyzed in aqueous solutions [17]. Sn@C nanoparticles are also promising anode materials for LIBs and SIBs due to their high theoretical capacities (993 mAh/g for $\text{Li}_{4.4}\text{Sn}$ and 847 mAh/g for $\text{Na}_{15}\text{Sn}_4$) and suitable working potentials [9,18–20]. Guided by theoretical analysis of the aerosol dynamics and reaction kinetics, Sn@C with different interior nanostructures of Sn in carbon matrices, similar to pitayas, pomegranates, and chestnuts, were synthesized by tuning the process parameters (Table 1). The pomegranate-structured Sn@C powders exhibit superior electrochemical performance as anode materials in LIBs and SIBs. CSP with *in-situ* solid-state reactions opens up new opportunities to produce uniform composition particles with complex structures from precursors without solubility limitations.

2. Experimental section

2.1. Sn@C fabrication by CSP

In the precursor, SnO_2 colloids (Nyacol, SN15ES) were added to an aqueous solution containing sucrose (Fisher Chemical), and then mixed with ethylene glycol (EG, Sigma-Aldrich, $\geq 99\%$) to form a 150-ml-precursor solution. The mass ratio of sucrose to SnO_2 colloids in the precursor was 20.2 (Sn@C pitaya), 12.1 (Sn@C pomegranate), and 0.3 (Sn@C chestnut), as shown in Table 1. Detailed calculation procedures to obtain the colloid concentration are presented in Note S1.

The prepared precursor was then atomized into droplets by a home built ultrasonic atomizer with a 1.7 MHz transducer. The droplets were

transported by N_2 gas through a quartz tube heated by a double furnace system (two furnaces connected in series, 81.3 cm in length). The set points of both furnaces were 750°C . The residence time of the reactor was 1.5 s for experiments to obtain Sn@C pitaya particles and 4.5 s for the fabrication of Sn@C pomegranate and chestnut particles. The residence time was tuned by changing the carrier gas flow rate into the system. At the end of the tube, the powders were cooled to 57°C by quench gas (N_2) and collected on a polytetrafluoroethylene (PTFE) filter (with a diameter of ~ 9.5 cm).

The residence time of our process was calculated by assuming our reactor is a plug-flow reactor, consisting 32 sub-units of identical length. By measuring the temperature in each sub-unit, the residence time of the process can be calculated, which has been reported in another paper of our group [14]. The residence time can be controlled by tuning the flow rate of carrier gas. The production rate of powders depends on the residence time. It varies between 0.1 g/h and 0.5 g/h.

2.2. Characterization

TEM was carried out using a JEOL 2100 LaB₆ TEM and a JEOL 2100 F FEG TEM equipped with Gatan image filter (GIF, Tridiem 863). The collected powders were dispersed in ethanol and sonicated for ~ 1 min. Then the mixture was added dropwise onto a lacey carbon film coated Cu grid in order to avoid the interference of C signal from the carbon film itself. SEM images were taken by a Hitachi SU-70 SEM. Similar to the TEM sample preparation, the ethanol-particle mixture was added dropwise onto a silicon wafer. In addition, a BRUKER D8 advance XRD was used to determine crystallographic information.

2.3. Electrode preparation and electrochemical measurement

Electrochemical measurements were performed using coin cells (CR2032) assembled in an argon-filled glove box (< 1 ppm of water and oxygen). To prepare the Sn@C electrode, Sn@C powders, carboxyl methyl cellulose (CMC), and carbon black with a mass ratio of 70: 20: 10 were magnetically stirred for over 5 h to ensure thorough mixing. The slurry was cast onto a thin copper foil and dried. Prior to cell fabrication, the electrodes were dried overnight at 80°C in a vacuum. The coin cells were assembled with lithium foil as the counter electrode, 1.0 M LiPF₆ solution in a mixture of dimethyl carbonate (DMC) and ethyl methyl carbonate (EMC) (1:1 volume ratio) with 10% fluoroethylene carbonate (FEC) for LIBs or 1.0 M NaClO_4 solution in a mixture of ethylene carbonate/dimethyl carbonate (EC/DMC, 1:1 by volume) for SIBs as the electrolyte, and a polypropylene film (Celgard3501, LLC Corp., USA) as the separator. The electrochemical

Table 1

Precursors to fabricate different structures of Sn@C particles.

		Pitaya	Pomegranate	Chestnut
Sucrose	[Sucrose] (mol/L)	2.0×10^{-1}	2.0×10^{-1}	1.0×10^{-2}
	Mass loading (kg/L)	7.0×10^{-2}	7.0×10^{-2}	3.5×10^{-3}
SnO_2	[SnO_2] (mol/L)	2.3×10^{-2}	3.8×10^{-2}	7.6×10^{-2}
	Mass loading (kg/L)	3.5×10^{-3}	5.8×10^{-3}	1.2×10^{-2}
	[SnO_2 colloid] (#/L)	1.1×10^{19}	1.9×10^{19}	3.8×10^{19}
Sucrose/ SnO_2	Molar ratio	8.9	5.2	0.13
	Mass ratio	20.2	12.1	0.3
Viscosity of precursor (mPa s)		2.24	2.14	1.63
Concentration of ethylene glycol (M)		4.8		

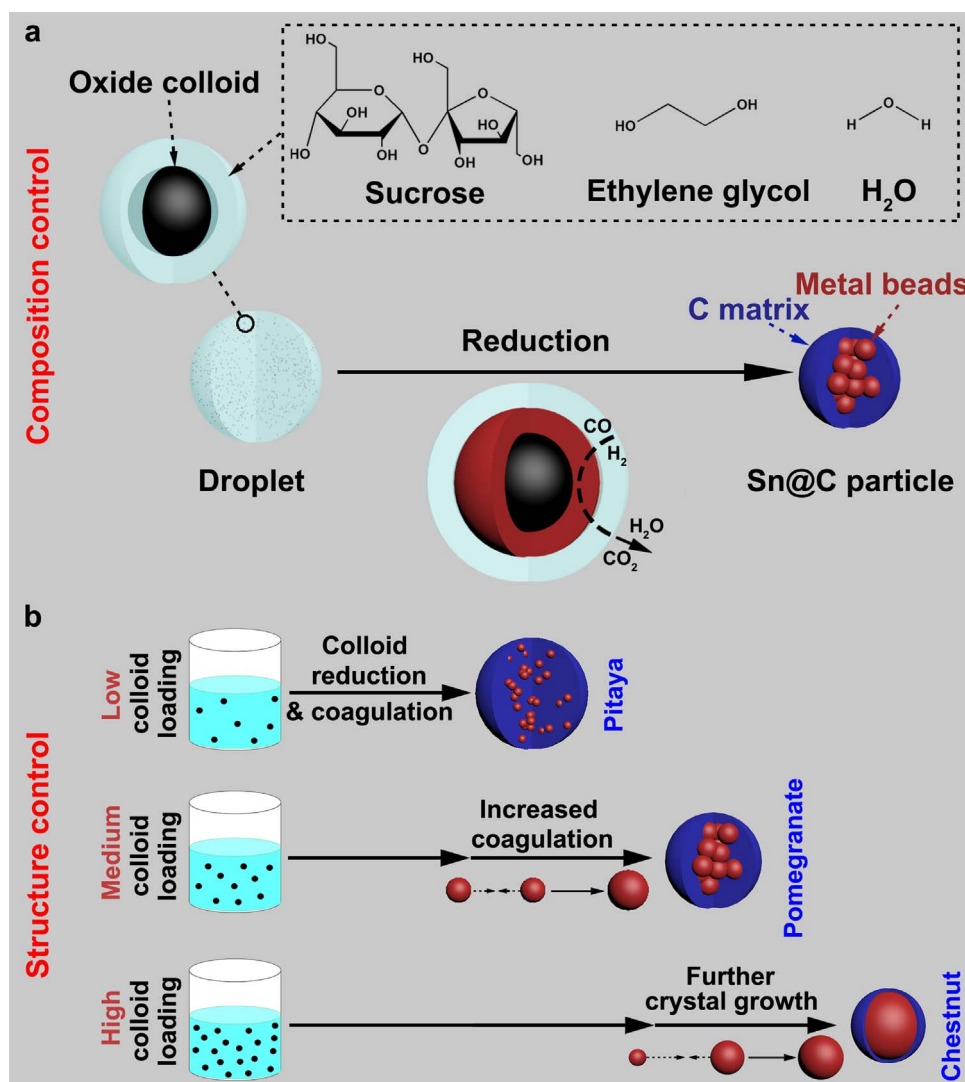


Fig. 2. Schematic illustration of the composition control (a) and structure control (b) in CSP.

properties of the Sn@C particles were studied with a multichannel battery-testing system (Arbin Instruments, TX, US), using charge/discharge galvanostatic cycling from 2.0 V to 0.01 V with the loading mass of $\sim 1.0 \text{ mg cm}^{-2}$. The specific capacity was calculated based on the mass of Sn@C powders. The electrochemical impedance spectrum and cyclic voltammetry measurements were carried out on an electrochemistry workstation (Solartron 1287/1260) at room temperature.

3. Results and discussion

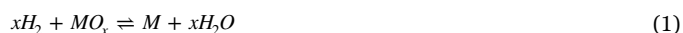
3.1. Aerosol dynamics and reaction kinetics in colloidal spray pyrolysis

In CSP, the aqueous precursor solution containing colloids, co-solvent, and stabilizer for colloids is first atomized into droplets. The droplets go through a series of processes including solvent evaporation, colloid reduction, and inter-colloid collision, forming product particles. The particle engineering of CSP involves both the oxide-colloid reduction and inter-colloid collision/coagulation processes (Fig. 2). The product composition is controlled by colloid reduction (Fig. 2a). The inter-colloid collision/coagulation determines the interior nanostructure of the product particles (Fig. 2b). Although both processes happen simultaneously during CSP, we can still model CSP in the ideal case in which the two processes are isolated.

3.1.1. Composition control

For the colloid reduction, the co-solvent is the main reducing agent in CSP during its decomposition. In a multiphase system, the diffusion of reactant gases through the colloids (Fig. 2a) may be difficult because of the mass transport resistance. For example, $D_{\text{gas-in-solid}}/D_{\text{liquid-in-liquid}}$ (diffusivity ratio) is as low as 10^{-5} at 25 °C [21,22]. In many cases, the densities of metals and their oxides are comparable. Therefore, the colloid reduction process can be simulated by the shrinking-core model [23]. In CSP, H₂ is mainly generated from co-solvent, which are uniformly dispersed in the droplets. The concentration of H₂ (C_{s,H_2}) was assumed to be uniform. The reduction process consists of mass transport of reactants and the chemical reaction.

Corresponding equations to calculate the time of the colloid reduction process were derived with detail procedures in Note S2. The chemical formula of the oxide (MO_x) reduction into metal (M) can be described as:



When the reduction is controlled by diffusion of H₂ through the metal ash outside the oxide core, the colloid reduction time is:

$$\tau = \frac{\rho_{\text{MO}_x} R^2}{6x D_{\text{C}_{s,H_2}}} (\text{diffusion controls}) \quad (2)$$

If chemical reaction between H₂ and the oxide core controls the CSP

process, the colloid reduction time can be calculated as:

$$\tau = \frac{\rho_{MOx} R}{x k_r C_{s,H_2}^n} \text{ (reaction controls)} \quad (3)$$

Here, D_e is diffusivity of H_2 in the metal layer. k_r is rate constant. n is reaction order. ρ_{MOx} is the density of metal oxides. R is the colloid radius. Based on Eqs. (2) and (3), the composition of product particles can be controlled. When the residence time of CSP process is larger than the time required for colloid reduction, the oxide colloids can be reduced completely into metal.

3.1.2. Structure control

The particle structure is controlled by inter-colloid collisions, as shown in Fig. 2b. In aerosol dynamics, the colloid collision frequency within individual droplets is a critical factor influencing the interior structure of the product particles [24]. The collision frequency (f) of colloids in the droplets can be expressed as [25]:

$$f = 8\pi D R N_{\infty}(t)^2 \quad (4)$$

where D is the viscosity of the media which can be estimated by Stokes-Einstein formula (Eq. (5)). Eq. (4) can be expanded into Eq. (6):

$$D = \frac{kT}{6\pi R\mu} \quad (5)$$

$$f = \frac{4}{3} \cdot \frac{kT}{\mu} \cdot N_{\infty}(t)^2 \quad (6)$$

k is Boltzmann constant. T is temperature. μ is the viscosity of the precursor. t is the time elapsed after the droplets enter the reactor. The collision frequency of colloids significantly depends on the initial colloid loading in the droplet ($N_{\infty}(0)$). A high colloid loading results in a high collision frequency, promoting the formation of large interior structures. Thus, precursor solutions with higher initial colloid loading favor denser particles, while lower colloid loading results in more porous particles composed of smaller beads as the interior structures [26–28]. Based on the analysis and Eqs. (4)–(6), we predict that the increasing colloid loading in the precursor solution may result in a growth of interior structure of the product particles, from dispersed small beads to large core, making the structure of product particles similar to pitaya, pomegranate, and chestnut in sequence, as illustrated in Fig. 2b.

3.2. Application of colloidal spray pyrolysis in fabricating Sn@C particles

To test the feasibility of CSP, it was applied to produce Sn@C particles from an aqueous precursor solution, containing SnO_2 colloids, ethylene glycol (EG) as the co-solvent, and sucrose as the stabilizer (Fig. 2a). The decomposition of EG can generate H_2 and CO gases during the processing [29,30]. Sucrose acts as a stabilizer for colloids in the precursor, carbon source, and reducing agent during its decomposition to carbon [31,32]. Therefore, both EG and sucrose provide H_2 . The precursor was atomized into 5 μm droplets (a volume mean diameter) by a 1.7 MHz ultrasonic generator [30]. The droplets were then transported by N_2 gas into two tube furnaces in series, both set at 750 °C. The SnO_2 colloids used in precursor solution have high crystallinity with lattice fringes attributed to the (200) plane of SnO_2 and narrow size distribution (number mean = 4.4 nm; standard deviation = 1.3 nm, Fig. 3a–c). The SnO_2 colloids-sucrose-EG aqueous precursor displayed stability with respect to precipitation for at least 2 h (Fig. S1), which is the prerequisite condition for uniform particle-to-particle composition and structure in products [8].

Firstly, the reduction time of SnO_2 colloids was calculated to understand the practicability of this process. The densities of Sn ($\rho_{Sn} = 7.31 \text{ g/cm}^3$, 20 °C) and SnO_2 ($\rho_{SnO_2} = 6.95 \text{ g/cm}^3$, 20 °C) are comparable [17]. Hence, the reduction time was determined based

on Eqs. (2) and (3) using shrinking-core model, as shown in Fig. 3d. The detailed simulation procedures are presented in Note S3. The precursor composition is listed in the Column Pomegranate in Table 1. The calculated results are summarized and plotted in Fig. 3e. The ratio of calculated colloid reduction time based on the diffusion-controlled model to that based on the reaction-controlled model is $\sim 10^{-7}$, when colloid radius is smaller than 75 nm. Therefore, chemical reaction is determined to be the rate-limiting step. In addition, when the residence times are 4.5 s, 1.5 s, or 0.92 s, the maximum radii of the SnO_2 colloids that can be completely reduced are 70 nm, 23 nm or 14 nm, respectively (Fig. 3e). These estimated radii are all larger than that of the SnO_2 colloids we used (2.2 nm), which means theoretically SnO_2 colloids can be completely converted to Sn by CSP.

Experimentally, the SnO_2 colloids have been successfully reduced in CSP with the conditions we used in the simulation mentioned above, as shown in Fig. 3f. All the peaks in the XRD diagram are pronounced and attributed to Sn (PDF No. 01-075-9188) without the existence of oxide phases. When the process residence time is 4.5 s, the product particles exhibit pomegranate-like structure with beads inside the particles (Figs. S2–3). The product particles change from spherical to fragmental structures with decreasing residence time, which is commonly observed in products by tuning the residence time of aerosol processes [14,24].

Guided by aerosol dynamics and Eqs. (4)–(6), we have also successfully controlled the interior structure of Sn@C particles by adjusting the initial colloid loading in the precursor (Table 1). Consistent with the theoretical prediction, when the initial SnO_2 -colloid loading increases from 1.1×10^{19} to 3.8×10^{19} colloids/L, the interior nanostructure in the carbon matrix shifts from small beads (pitaya-structure in Fig. 4a,d,g), through more coagulated beads (pomegranate-structure in Fig. 4b,h,k), to large cores (chestnut-structure in Fig. 4c,i,o), as clearly demonstrated in TEM images and their corresponding elemental mappings. From both TEM and SEM images (Fig. S4), particle size distributions are summarized in Fig. 4p–v. The average size of Sn beads in C matrix is 16 nm (pitaya-structured), 24 nm (pomegranate-structured), and 139 nm (chestnut-structured). The increasing average size of Sn beads with colloid loading confirms that inter-colloid collision frequency increased with initial colloid loading. Sn@C particles show spherical morphology with average particle diameter decreasing from 340 nm (pitaya-structured), through 301 nm (pomegranate-structured), to 139 nm (chestnut-structured). The mass fraction of Sn in the Sn@C particles increases from 77% (pitaya-structured), through 83% (pomegranate-structured), to 89% (chestnut-structured) with decreasing the mass ratio of sucrose to SnO_2 in the precursor, as shown in Fig. S5. Moreover, the pitaya-structured particles have the highest surface area and chestnut-structured particles display the lowest surface area, as depicted in Fig. S6.

The formation of crystal Sn and amorphous carbon in all three types of Sn@C particles is supported by the theoretical analysis on the colloid-reduction (Table S1) and confirmed by the XRD measurement (Fig. S7). Although the colloid loading varies between the three conditions to obtain different structured Sn@C particles, the theoretical colloid reduction times are all smaller than the process residence times, suggesting the colloids can be completely reduced by the CSP (Table S1). The XRD patterns further validate this hypothesis with noticeable peaks from Sn phase and the absent of oxide phases (Fig. S7). The full-width at half-maximum (FWHM) of the main peak at 30.8° decreased from 0.27 (pitaya-structured), through 0.25 (pomegranate-structured), to 0.18 (chestnut-structured), indicating that the Sn@C chestnut particles have the largest Sn crystalline domain based on Scherrer equation. Sn@C chestnut has the greatest degree of crystallinity, which is attributed to the fastest nucleation and crystal growth among the Sn@C particle production processes. This is also consistent with the aerosol dynamic analysis that the high initial colloid loading contributes to the high frequency of inter-colloid collision.

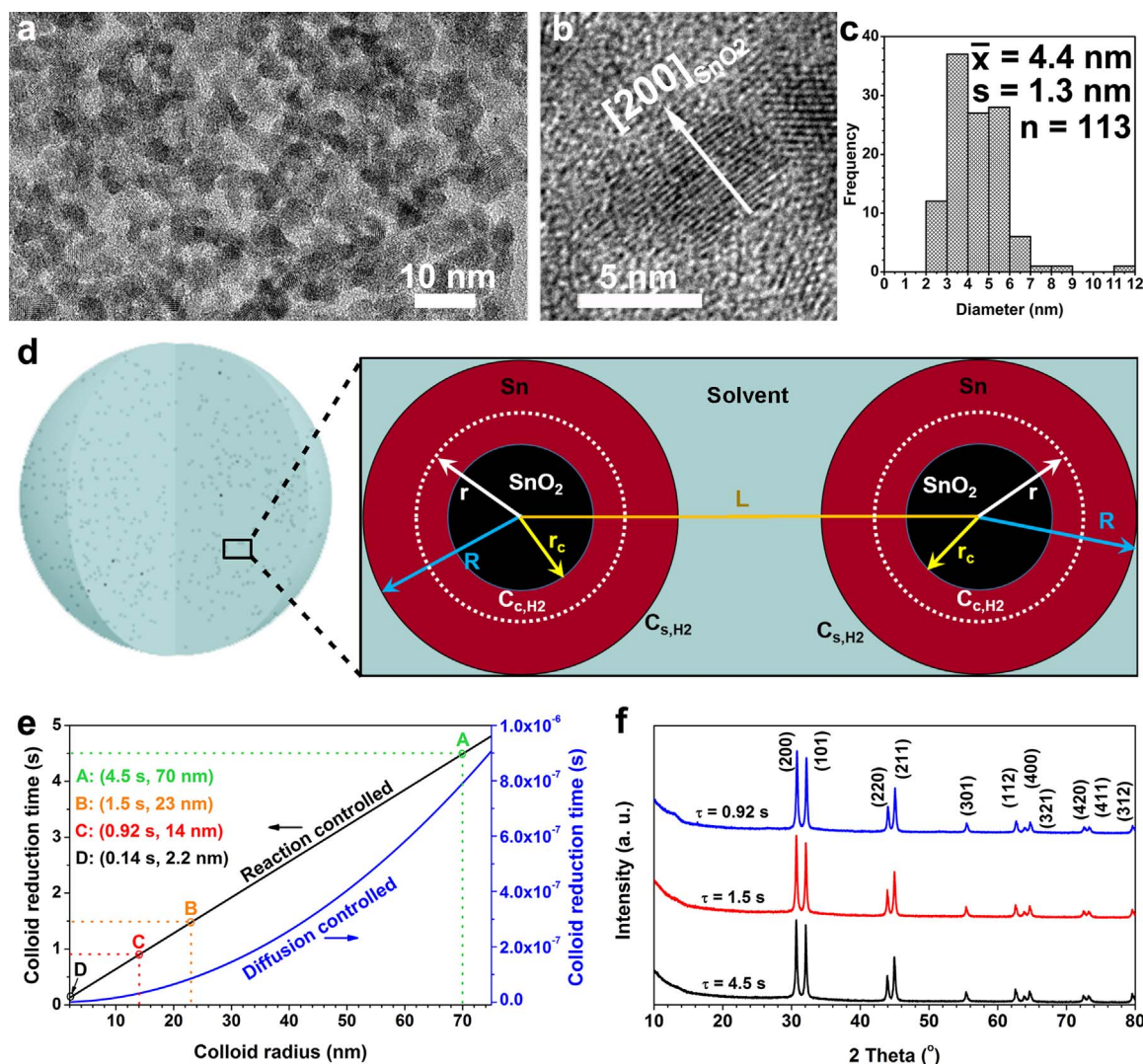


Fig. 3. Composition control of the product particles by colloidal spray pyrolysis. (a–b) TEM image of the SnO_2 colloids used in the precursor (a) with HRTEM image (b). (c) Diameter distribution of SnO_2 colloids with mean diameter, standard deviation, and sample size. (d) Schematic of parameters used in calculating the time of colloidal reduction in colloidal spray pyrolysis. (e) The time required to reduce a SnO_2 colloid as a function of initial colloid diameter, based on reaction-controlled model (left y-axis) and diffusion-controlled model (right y-axis). (f) XRD diagram of powders obtained at 750 °C when the residence time of the process is 4.5 s (black curve), 1.5 s (red curve), and 0.92 s (blue curve). (For interpretation of the references to color in this figure legend, the reader is referred to the web version of this article.)

To validate this aerosol dynamic analysis, we further changed the initial SnO_2 colloid loading to 6.1 (mass ratio of sucrose to SnO_2 colloids, Table S2), a condition between those to obtain Sn@C pomegranate (12.1) and chestnut (0.3) particles. The Sn@C particles fabricated at this condition (termed as intermediate) display a mix of pomegranate-structured and chestnut-structured particles (Fig. S8), which is consistent with our theoretical analysis. In the XRD pattern of Sn@C intermediate particles (Fig. S7), the FWHM of the main peak at 30.8° is 0.24, which is also between those of the Sn@C pomegranate and chestnut powders, consistent with the SnO_2 loading in the precursor.

It is worth mentioning that the model in the above discussion is based on the ideal situation where the colloid reduction and inter-colloid collision/coagulation are isolated procedures. In reality, these steps happen simultaneously, which means the size of colloids is increasing due to coagulation during the reduction. Therefore, the actual radius of the colloids that needs to be reduced is larger than the radius of the colloids added into the precursors. A precursor solution was also processed under the same conditions to obtain Sn@C pomegranate-structured particles but without the addition of EG ($C_{s,H2} = 1.5$ M). Based on the reaction kinetics, the colloid reduction

time is 0.3 s, which is smaller than the process residence time (4.5 s). Thus, theoretically, SnO_2 colloids should be completely reduced. However, residual SnO_2 exists in Sn@C particles synthesized from the EG-free precursor, as demonstrated by a weak SnO_2 peak in the XRD diagram (Fig. S9). This phenomenon implies that EG is the main reducing agent in the CSP process and is crucial in tuning the composition of the products. Different from adding highly flammable H_2 gas as the reducing agent in the conventional spray pyrolysis [9], we used EG as a reducing agent in CSP, which can address the potential safety concerns. In addition, the *in-situ* formed H_2 from the decomposition of EG can be controlled by tuning the EG concentration in the precursor solution. Therefore, using EG as the cosolvent and reducing agent is an efficient strategy, which was also confirmed by previous works [14,30]. Furthermore, the coagulation of the colloids increases the difficulty of complete reduction of the colloids. However, our model can still be applied to screen the colloids that can be processed by CSP and pre-design product structures.

The possibility of collision between the product particles should also be considered. The collision rates between Sn@C product particles in all three scenarios were also calculated and shown in Table S3 and Note S4. Significantly longer collision/coagulation half-lives than

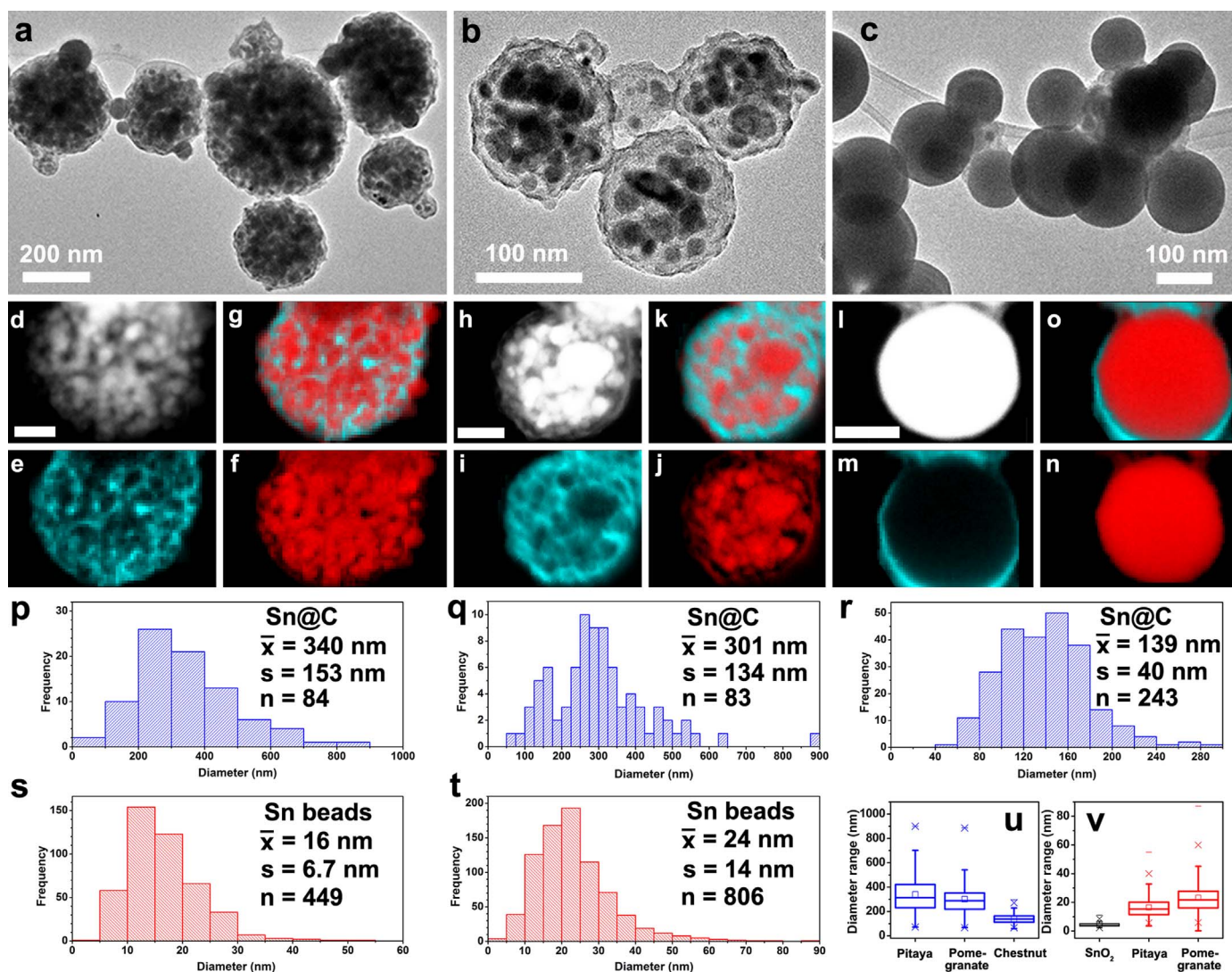


Fig. 4. Structure control of the product particles by colloidal spray pyrolysis. (a-c) TEM images of pitaya-structured (a), pomegranate-structured (b), and chestnut-structured (c) particles. (d-n) STEM-HAADF image and EELS elemental mappings of C signal, Sn signal, and overlap result of Sn@C pitaya (d-f, respectively), pomegranate (h-k, respectively), and chestnut (l-o, respectively) particles. The scale bars in STEM-HAADF images are 50 nm. (p-t) Statistical summaries of Sn@C particle and interior Sn bead diameters of pitaya-structured (p,s, respectively), pomegranate-structured (q,t, respectively), and chestnut-structured (r) particles with mean values, standard deviations, and sample sizes. (u-v) Box plots to summarize the size distributions of Sn@C particles (u) and Sn beads (v).

process residence times indicate negligible collisions between Sn@C particles, verifying the one-droplet-one-particle model [33].

As discussed in above, sucrose produces reducing gases during its decomposition and also results in the formation of carbon [31], which serves as the framework in Sn@C particles. As shown in Fig. 5a-h, the edge of the chestnut-structured particles is encapsulated by crystalline carbon layers, revealing long-range ordered lattice fringes with spacing of 3.1–3.3 Å (Fig. 5a-c). It is consistent with the results that the inter-layer distance in the stacked carbon layers is around 3.3 Å [34,35]. The strong C signal in electron energy loss spectroscopy (EELS) spectra (Fig. 5i-j) validates the Sn_{core}C_{shell} structure of chestnut-like particles. The EELS spectral feature of C K-edge from both the edge and center of the chestnut particle display clear π^* peaks at ~ 284 eV (Fig. 5i-j), which are excited from C atoms with the sp^2 coordination environment [36]. For the Sn@C pomegranate, the stacking of C layers can only be found in the localized region (Fig. 5d-f). In EELS spectra, weak π^* signals and peaks are observed in Fig. 5i-j. For the pitaya-structured particles, the crystalline carbon layers are difficult to be observed around the Sn beads (Fig. 5g-h). π^* signals and peaks are also insignificant in EELS spectra (Fig. 5i-j). Raman spectra of Sn@C pitaya, pomegranate, and chestnut are consistent with TEM and

EELS observations with Sn@C chestnut showing the highest D/G peak ratio and most pronounced 2D peak (Fig. S10). Contrarily, Sn@C pitaya exhibits the lowest D/G peak ratio and negligible 2D peak.

Compared to reported Sn-based functional particle engineering, CSP exhibits distinguished advantages including simple operating procedures, short processing time, mild reducing conditions, and better control of product structure and composition (Table S4). The increasing concentration of co-solvent in the precursor solution can tune the product from oxides to metals. Moreover, the desired product structure (pitaya-like, pomegranate-like, or chestnut-like) can be achieved by adjusting the colloid loading in the precursor solution. Based on Eqs. (2) and (3), the product composition processed by CSP significantly depends on the size of input colloids (R), material properties (ρ_{MOx} , D_e , k_r), the concentration of reducing agent ($C_{s,H2}$), and the process residence time. Generally, oxide colloids with small size, low density, high diffusion coefficient of reducing gas in the colloids, and high reaction coefficient of reduction are easily reduced to metals. For example, with the same colloid size and concentration of reducing agent as we used in this work, oxide colloids with higher reaction coefficients, which can be found in Ellingham diagram [37], may also be reduced to metals by CSP.

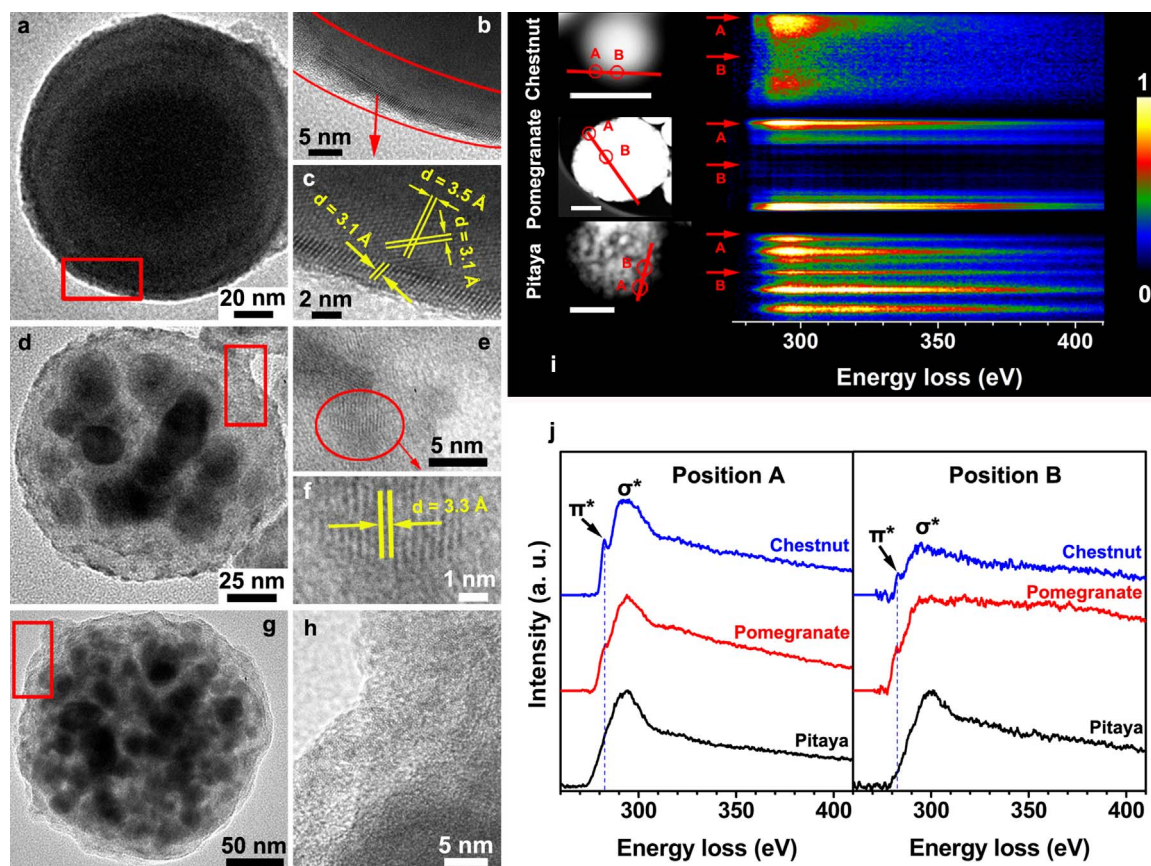


Fig. 5. Carbon frames in Sn@C particles. (a–h) TEM images of chestnut-structured (a), pomegranate-structured (d), and pitaya-structured (g) particles with its corresponding HRTEM images (b)–(c), (e)–(f), and (h), respectively. The HRTEM images were taken from the areas marked by red color boxes. (c,f) Higher magnification images of areas in (b) and (e), respectively. (i) STEM-HAADF images (left) and EELS line scan results (right) of chestnut-, pomegranate-, and pitaya-structured particles (from top to bottom). The scale bars in HAADF images are 100 nm. (j) EELS spectra of C K-edge extracted from position A (left) and B (right) of (i).

3.3. Electrochemical performance of Sn@C anodes in LIBs

The Sn@C particles are promising anode materials for LIBs because Sn is an electrochemically active component with a high capacity (The theoretical specific capacity of Sn is 993 mAh g^{-1} for LIBs) [38,39] and the elastic carbon matrix can effectively act as a sponge to alleviate the mechanical stress accompanying the volume change of Sn, which is a critical factor to influence the electrochemical performance of Sn-based anodes [38,40–42]. The interior nanostructures of the three Sn@C particles produced by CSP have significant impacts on the initial Coulombic efficiency (CE) and cycling stability, as shown in Fig. 6. The voltage profiles in the voltage range of 0.01–2 V of the three Sn@C anodes in the first charge/discharge cycles for LIBs are obtained at a current of 1/10 C (1 C = 993 mA/g). Sn@C pomegranate anode displays the highest initial CE of 74.3% (Fig. 6a). The electrochemical properties of the three Sn@C anodes in LIBs were also evaluated by cyclic voltammetry (CV) as shown in Fig. S11. Broad reduction peaks at $\sim 0.85 \text{ V}$ are observed in the first cathodic scan of the three Sn@C anodes, but disappear in the subsequent cycles, which could be ascribed to the formation of a solid electrolyte interphase (SEI) layer at the electrode/electrolyte interface [43,44]. In the CV curve, e.g., Sn@C pomegranate anode, three small reduction peaks at 0.31, 0.37, and 0.61 V can be attributed to the insertion of Li into Sn to form Li_xSn alloys. By comparison, the anodic CV scan of Sn@C pomegranate anode shows four peaks at 0.48, 0.64, 0.73, and 0.79 V attributed to $\text{Li}_{22}\text{Sn}_5$ to Li_7Sn_3 , LiSn , Li_2Sn_5 , and Sn, respectively, suggesting the reversible delithiation reaction of amorphous Li_xSn phase to the amorphous Sn [38]. Both cathodic and anodic curves overlap in the following CV scans, indicating the high reversibility and excellent overall cycling stability of the Sn@C anodes.

The rate performance of three Sn@C anodes at different current densities ranging from 1/20 C to 5 C is illustrated in Fig. 6b. Sn@C pomegranate anode exhibits a high capacity, about 500 mAh g^{-1} even at 5 C. Furthermore, a capacity of 865 mAh g^{-1} can be retained when the current density is reduced back to 1/10 C after charging/discharging for 35 cycles at various current densities, demonstrating that the Sn@C pomegranate anode is highly robust and can tolerate the current changes. The exceptional rate capability of the Sn@C pomegranate makes it promising for practical applications that demand high power capacity and energy density. Contrarily, the Sn@C chestnut displays poor initial CE and rate performance (Fig. 6a–b), because the solid Sn@C structure is not able to tolerate the expansion of large Sn core during the lithiation process after long-term cycling. The electrochemical performance of Sn@C anodes in the voltage range of 0.01–1.0 V has also verified that Sn@C pomegranate anode has higher capacity ($\sim 757 \text{ mAh g}^{-1}$) and relatively superior stability (Fig. S12a–c) than the Sn@C chestnut anode. A lower capacity of Sn anode was obtained because of the decreasing operation voltage range. After 10 cycles at 0.1 C, the distinct charge/discharge plateaus were obviously observed due to the delithiation/lithiation reaction of amorphous Li_xSn phase (Fig. S12d–f), and the capacity of Sn@C pomegranate anode could also retain 738 mAh g^{-1} after 10 cycles (97.5% capacity retention of the second cycle). The irreversible capacity loss of Sn@C composites occurred in the first cycle due to the SEI formation.

The reaction kinetics of the three Sn@C anodes during lithiation/delithiation were evaluated using electrochemical impedance spectroscopy (EIS) after full delithiation to 2 V during the first cycle. As shown in Fig. 6c, the high-frequency semicircle corresponds to R_{int} (interface resistance), including R_{ct} (charge transfer resistance) and R_{SEI} (SEI resistance) ($R_{\text{int}} = R_{\text{SEI}} + R_{\text{ct}}$), while the low-frequency line represents

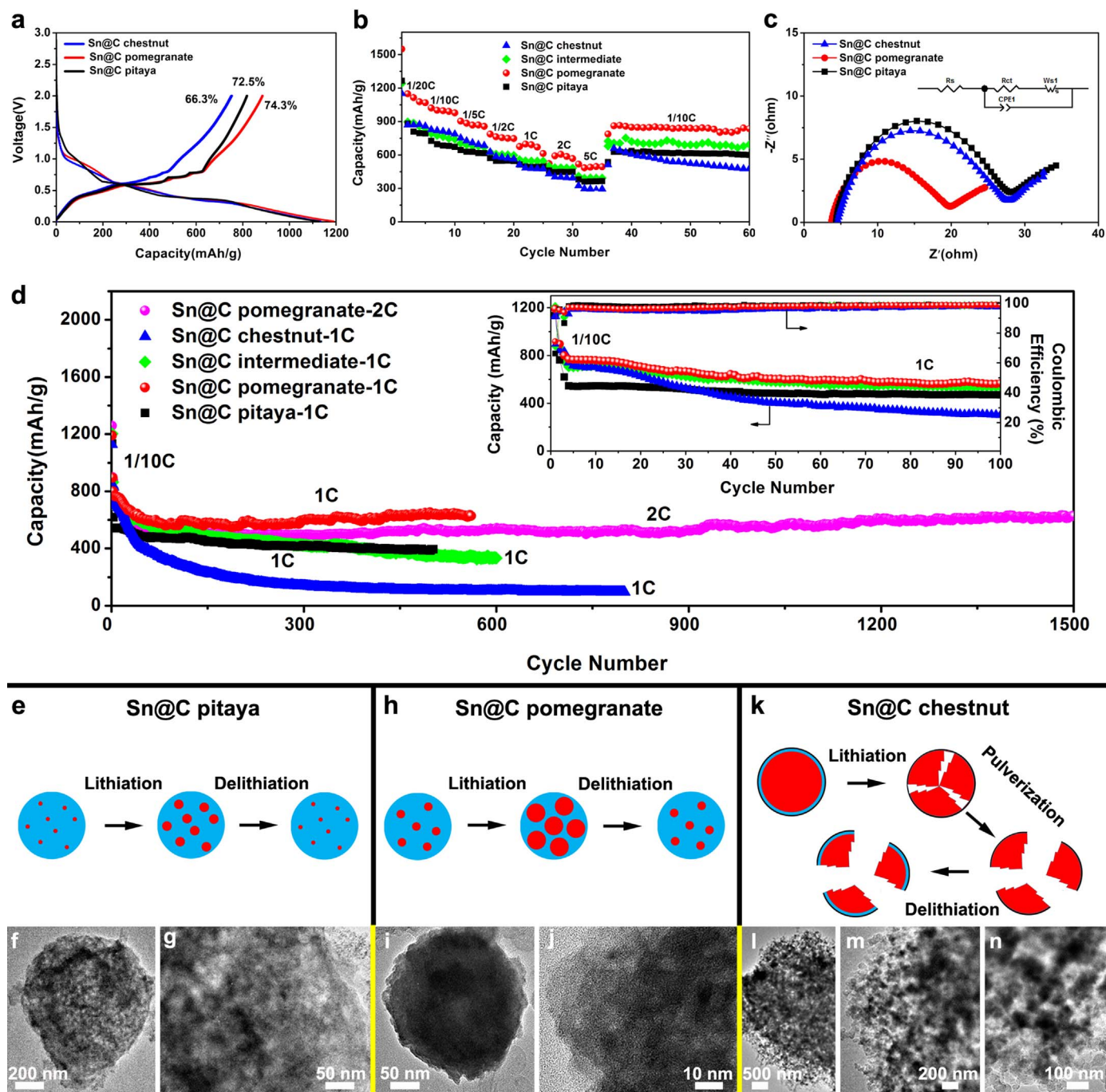


Fig. 6. Electrochemical performance of LIBs anodes fabricated from Sn@C particles. (a) Charge/discharge profiles of the Sn@C pitaya, pomegranate, and chestnut anodes at the first cycle. (b) Rate capacity performance of the Sn@C anodes between 0.01 V and 2.0 V at various rates (1/20–5 C). (c) Nyquist plots of the electrodes of the Sn@C anodes at 2 V. (Z' and Z'' denote real and imaginary parts, respectively). (d) Long-term cycling stability of the Sn@C electrodes at a current density of 1/10 C for the initial three cycles and at 1 C or 2 C for the following cycles. The inset is cycling performance of the Sn@C anodes for the initial 100 cycles at 1 C. (e–n) Schematic summaries of structural evolution during lithiation/delithiation and TEM images of pitaya-structured (e–g), pomegranate-structured (h–j), and chestnut-structured (k–n) particles in anodes after 100 cycles in rate performance test.

ion diffusion resistance [45,46]. The diameter of the semicircle at high frequency for the Sn@C pomegranate anode is smaller than those of the Sn@C pitaya and chestnut anodes. As summarized in Table S5, the lower interface impedance of the pomegranate Sn@C anode (14.15 Ω) compared with those of Sn@C pitaya (21.85 Ω) and chestnut (23.26 Ω) can be attributed to an enhanced charge transfer reaction due to both relatively small Sn@C particles size (301 nm) and well-dispersed Sn particles in elastic carbon matrix (Fig. 4b,u,v). This is consistent with the order of the rate capabilities of the Sn@C electrodes as shown in Fig. 6b. Moreover, electron transfer ability is enhanced by the elastic carbon, resulting in better rate performance and connection of active

materials [47].

The long-term cycling stability of three Sn@C anodes was evaluated at 1 C after activation for the initial 3 cycles at 1/10 C (inset of Fig. 6d). The capacity of Sn@C chestnut anode endured the most significant capacity decay at the initial 100 cycles. In contrast, the Sn@C pitaya and pomegranate anodes retained highly stable electrochemical performance after 100 charge/discharge cycles. Similarly, the Sn@C pitaya also exhibited good cycling stability due to its nanostructured Sn and elastic carbon framework, which can support the large volume change during lithiation process, after capacity decay in first 5 cycles. Long-term cycling performance (Fig. 6d) of the Sn@C electrodes were

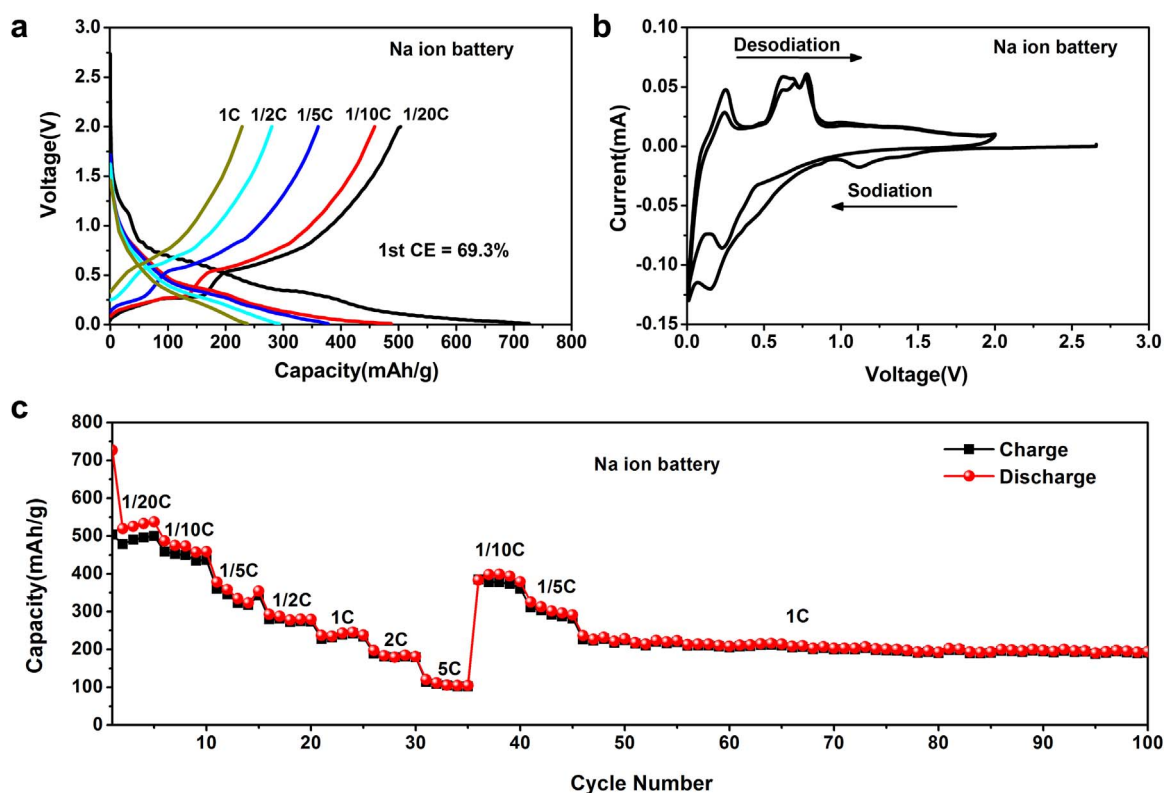


Fig. 7. Electrochemical performance of SIBs anodes fabricated from Sn@C pomegranate particles. (a) Charge/discharge profiles for Sn@C pomegranate anode at different current densities. (b) Cyclic voltammetry curves of Sn@C pomegranate anode in SIB at a scan rate of 0.1 mV/s. (c) Rate capability of Sn@C pomegranate anode in SIB.

evaluated at a high rate of 1 C and 2 C. The capacity retention of Sn@C pomegranate anode can be maintained at 627.9 mAh/g even after 1500 cycles, corresponding to 88.5% capacity retention at 2 C. In Table S6, a detailed comparison is presented to show that the Sn@C pomegranate anode has superior electrochemical performance when compared with the reported Sn-based anodes in the similar operation voltage range. The Sn@C pitaya anode also displayed a stable cycling performance, which could be maintained at 400 mAh g⁻¹ after 500 cycles, about 72.8% of initial capacity at 1 C. Contrarily, for the Sn@C chestnut anode, the capacity dropped rapidly after only 200 cycles to less than 200 mAh g⁻¹. Therefore, the electrochemical performance of Sn@C in LIBs could be effectively controlled by CSP.

As reported, the volume expansion of Sn could be ~ 260% [38,40–42], thus the superior cycling and rate performance of Sn@C pomegranate anodes are attributed to the excellent structural stability, originated from the well distributed Sn beads within relative small Sn@C particles. To effectively accommodate for the volume change in Sn@C, both diameters of Sn@C particle and interior Sn bead should be small, while the Sn@C particle size is more crucial in cycling stability (Fig. 6e,h,k). As demonstrated in Fig. 4, the pomegranate-structured particles have smaller Sn@C particle size but larger interior Sn size (301 nm and 24 nm, respectively) than pitaya-structured particles (340 nm and 16 nm, respectively). The smaller pomegranate-structured particle in Sn@C pomegranate anode ensures better cycling stability than Sn@C pitaya anode. Although chestnut-structured particles have the smallest Sn@C particle size (139 nm), the significantly large Sn core (close to 139 nm) can seriously damage the Sn@C composite particles (Fig. 6k), resulting in quick capacity decay. Therefore, the pomegranate-structured Sn@C particles have sufficient and well-defined internal space to tolerate the expansion of Sn beads in the elastic carbon frames without deteriorating the structural integrity of the anode (Fig. 6h). To test this hypothesis, the particle structures of Sn@C anodes were characterized by TEM (Fig. 6) and SEM (Fig. S13) after 100 cycles in rate performance tests. The Sn@C pitaya and

pomegranate anodes maintained stable structures with spherical shape of Sn@C particles, which are similar to those before the electrochemical test (Fig. 6f–g and i–j, respectively). However, cracking or fracture in the Sn@C chestnut anode was observed as shown in Fig. 6l–n.

To further validate our theory, the Sn@C intermediate anode was tested for electrochemical performance. Since Sn@C intermediate particles are comprised of structures between pomegranate-structured and chestnut-structured particles, Sn@C intermediate anode in theory should have a structural and cycling stability between Sn@C pomegranate and chestnut anodes, which was verified experimentally in the electrochemical performance testing (Fig. 6b,d) and the structure characterization of the anode after the electrochemical test (Fig. S14).

3.4. Electrochemical performance of Sn@C pomegranate anodes in SIBs

Although the volume expansion of Sn-based anodes in SIBs is 420% [48], the Sn@C pomegranate anodes for SIBs present excellent electrochemical performance, as shown in Fig. 7. The galvanostatic discharge/charge profiles at various current densities in rate-capability tests are depicted in Fig. 7a. The first discharge/charge capacities of Sn@C pomegranate anode are 726.8 and 503.6 mAh g⁻¹ at 0.05 C (1 C = 847 mA/g). Even at increased current densities, the discharge/charge profiles of Sn@C pomegranate anodes in SIB still exhibit significant voltage plateaus corresponding to the sodiation/desodiation process (Fig. 7a). Impressively, the first CE reaches 69.3%, which is relatively high compared to reported Sn@C anodes in SIBs [45,49–51], confirming that the Sn@C pomegranate structure alleviates detrimental reactions between Sn and electrolyte during the sodiation process. However, the first cycle capacity loss could not be avoided because of the formation of SEI layer, which is consistent with the CV curve of the Sn@C pomegranate anode (Fig. 7b) and other previous studies of Sn@C anodes in SIBs [51,52]. In Fig. 7c, Sn@C pomegranate anode in SIBs was galvanostatically discharged and charged at different current

densities from 0.05 C to 5 C. The cell could deliver 487.3, 378.0, 293, 237.6, 197.2, 120.4 mAh g⁻¹ at 0.1 C, 0.2 C, 0.5 C, 1 C, 2 C and 5 C, respectively. In particular, the capacity could be recovered to its original value when the rates were set back to 0.1 C, 0.2 C and even 1 C after 100 cycles, respectively. This clearly substantiates that the sodiation reaction in Sn@C pomegranate anode is highly reversible.

Furthermore, to better understand the thermodynamics and reaction kinetics of Sn@C pomegranate anodes during the electrochemical test in LIBs and SIBs, the galvanostatic intermittent titration technique (GITT) measurements have been performed, as shown in Fig. S15. The quasi-equilibrium for lithiation in LIBs is from 0.14 V to 0.07 V (Fig. S15a), lower than that of sodiation (0.30–0.11 V) in SIBs (Fig. S15b). The average resistance of the in Sn@C pomegranate anode in SIBs is more than 2 times higher than that in LIBs (Fig. S15f,g), indicating the relatively poor electrochemical sodiation/desodiation kinetics in SIBs compared with LIBs, which explain the inferior electrochemical performance of SIBs than that of LIBs.

4. Conclusion

We have successfully developed a general strategy to synthesize multicomponent particles by CSP. This process is fundamentally different from the conventional aerosol processes where only highly soluble salts, pure organic solvents, and extreme reducing conditions are favored. By applying CSP, a wider range of functional materials can be produced at low cost, with safer process conditions, and facile operating procedures. A specific example of the application of CSP was presented to generate Sn@C particles for LIBs and SIBs anodes, which is difficult to obtain by conventional methods. Although this work only utilized Sn as the example, CSP is applicable to other elements. Furthermore, the model we developed provides a better understanding of the particle formation mechanism in the aerosol processes. Meanwhile, this model can also be utilized to prescreen the colloids that can be processed by CSP and design the process variables to obtain desired products. With the guidance of theoretical analysis of the colloid-reduction kinetics and aerosol dynamics, Sn@C particles with controllable interior structures (pitaya, pomegranate and chestnut-structured) were produced through complete reduction of the SnO₂ colloids by *in-situ* solid-state reaction. The Sn@C pomegranate anodes displayed excellent battery performance with 88.5% (1500 cycles; 2 C) capacity retention for LIBs and exhibited superior rate capability for SIBs, which are among the best performance for Sn-based anodes reported to date.

Acknowledgements

This work was supported by i) National Science Foundation (CBET-1336581), ii) National Natural Science Foundation of China (Grant no. 51504234), and iii) Zhejiang Provincial Natural Science Foundation of China (Grant no. LY16E040001). The authors acknowledge the support of the Maryland NanoCenter and its AIMLab and FabLab.

Appendix A. Supporting information

Supplementary data associated with this article can be found in the online version at doi:10.1016/j.ensm.2017.12.021.

References

- [1] F. Lin, D. Nordlund, Y. Li, M.K. Quan, L. Cheng, T.-C. Weng, Y. Liu, H.L. Xin, M.M. Doeff, Metal segregation in hierarchically structured cathode materials for high-energy lithium batteries, *Nat. Energy* 1 (2016) 15004.
- [2] D.S. Jung, T.H. Hwang, J.H. Lee, H.Y. Koo, R.A. Shaker, R. Kahrman, Y.N. Jo, M.-S. Park, J.W. Choi, Hierarchical porous carbon by ultrasonic spray pyrolysis yields stable cycling in lithium–sulfur battery, *Nano Lett.* 14 (2014) 4418–4425.
- [3] Y. Zhu, S.H. Choi, X. Fan, J. Shin, Z. Ma, M.R. Zachariah, J.W. Choi, C. Wang, Recent progress on spray pyrolysis for high performance electrode materials in lithium and sodium rechargeable batteries, *Adv. Energy Mater.* 7 (2017) 1601578.
- [4] R. Koirala, S.E. Pratsinis, A. Baiker, Synthesis of catalytic materials in flames: opportunities and challenges, *Chem. Soc. Rev.* 45 (11) (2016) 3053–3068.
- [5] M.V. Reddy, G.V. Subba Rao, B.V.R. Chowdari, Metal oxides and oxyanions as anode materials for Li ion batteries, *Chem. Rev.* 113 (2013) 5364–5457.
- [6] S.H. Choi, Y.N. Ko, J.K. Lee, Y.C. Kang, 3D MoS₂-graphene microspheres consisting of multiple nanospheres with superior sodium ion storage properties, *Adv. Funct. Mater.* 25 (2015) 1780–1788.
- [7] J.H. Bang, K.S. Suslick, Applications of ultrasound to the synthesis of nanostructured materials, *Adv. Mater.* 22 (2010) 1039–1059.
- [8] A. Gurav, T. Kodas, T. Pluym, Y. Xiong, Aerosol processing of materials, *Aerosol Sci. Technol.* 19 (1993) 411–452.
- [9] Y. Xu, Q. Liu, Y. Zhu, Y. Liu, A. Langrock, M.R. Zachariah, C. Wang, Uniform nano-Sn/C composite anodes for lithium ion batteries, *Nano Lett.* 13 (2013) 470–474.
- [10] N. Zhang, Q. Zhao, X. Han, J. Yang, J. Chen, Pitaya-like Sn@C nanocomposites as high-rate and long-life anode for lithium-ion batteries, *Nanoscale* 6 (2014) 2827–2832.
- [11] Y.J. Hong, Y.C. Kang, One-pot synthesis of core–shell-structured tin oxide–carbon composite powders by spray pyrolysis for use as anode materials in Li-ion batteries, *Carbon* 88 (2015) 262–269.
- [12] B.N. Joshi, S. An, Y.I. Kim, E.P. Samuel, K.Y. Song, I.W. Seong, S.S. Al-Deyab, M.T. Swihart, W.Y. Yoon, S.S. Yoon, Flexible free-standing Fe₂O₃-SnO₂-carbon nanofiber composites for Li ion battery anodes, *J. Alloy. Compd.* 700 (2017) 259–266.
- [13] C.L. Yaws, *Chemical Properties Handbook*, McGraw-Hill, New York, 1999.
- [14] Y. Liang, R. Felix, H. Glicksman, S. Ehrman, Cu-Sn binary metal particle generation by spray pyrolysis, *Aerosol Sci. Technol.* 51 (2017) 430–442.
- [15] D.S. Jung, T.H. Hwang, S.B. Park, J.W. Choi, Spray drying method for large-scale and high-performance silicon negative electrodes in Li-ion batteries, *Nano Lett.* 13 (2013) 2092–2097.
- [16] C. Boissiere, D. Grosso, A. Chaumonnot, L. Nicole, C. Sanchez, Aerosol route to functional nanostructured inorganic and hybrid porous materials, *Adv. Mater.* 23 (2011) 599–623.
- [17] D.L. Perry, *Handbook of Inorganic Compounds*, CRC press, 2011.
- [18] Q. Chen, K. Sieradzki, Spontaneous evolution of bicontinuous nanostructures in dealloyed Li-based systems, *Nat. Mater.* 12 (2013) 1102–1106.
- [19] H.S. Im, Y.J. Cho, Y.R. Lim, C.S. Jung, D.M. Jang, J. Park, F. Shojaei, H.S. Kang, Phase evolution of tin nanocrystals in lithium ion batteries, *ACS Nano* 7 (2013) 11103–11111.
- [20] H. Tian, F. Xin, X. Wang, W. He, W. Han, High capacity group-iv elements (Si, Ge, Sn) based anodes for lithium-ion batteries, *J. Mater.* 1 (2015) 153–169.
- [21] A.S. Nowick, *Diffusion in Solids: Recent Developments*, Elsevier, New York, 2012.
- [22] W.M. Deen, *Analysis of Transport Phenomena (Topics in Chemical Engineering)*, Oxford University Press, New York, 1998.
- [23] O. Levenspiel, *Chemical Reaction Engineering*, Wiley, New York, 1999.
- [24] A.B.D. Nandiyanto, K. Okuyama, Progress in developing spray-drying methods for the production of controlled morphology particles: from the nanometer to submicrometer size ranges, *Adv. Powder Technol.* 22 (2011) 1–19.
- [25] V.G. Levich, *Physicochemical Hydrodynamics*, Prentice Hall, New Jersey, 1962.
- [26] F. Iskandar, S.-G. Kim, A.B.D. Nandiyanto, Y. Kaihatsu, T. Ogi, K. Okuyama, Direct synthesis of HBN/MWCNT composite particles using spray pyrolysis, *J. Alloy. Compd.* 471 (2009) 166–171.
- [27] J. Bahadur, D. Sen, S. Mazumder, B. Paul, A. Khan, G. Ghosh, Evaporation-induced self assembly of nanoparticles in non-buckling regime: volume fraction dependent packing, *J. Colloid Interface Sci.* 351 (2010) 357–364.
- [28] W.-N. Wang, W. Widiyastuti, I. Wuled Lenggoro, T. Oh Kim, K. Okuyama, Photoluminescence optimization of luminescent nanocomposites fabricated by spray pyrolysis of a colloid-solution precursor, *J. Electrochem. Soc.* 154 (2007) J121–J128.
- [29] H. Yue, Y. Zhao, X. Ma, J. Gong, Ethylene glycol: properties, synthesis, and applications, *Chem. Soc. Rev.* 41 (2012) 4218–4244.
- [30] K. Zhong, G. Peabody, E. Blankenhorn, H. Glicksman, S. Ehrman, Spray pyrolysis of phase pure AgCu particles using organic cosolvents, *J. Mater. Res.* 28 (2013) 2753–2761.
- [31] Y.K. Cho, K.Y. Jung, H. Lee, S. Heo, Synthesis and characterization of C/Cu core-shell particles by hydrogen-free spray pyrolysis assisted with citric acid and sucrose, *Mater. Res. Bull.* 48 (2013) 3424–3430.
- [32] K. Wang, R. Cai, T. Yuan, X. Yu, R. Ran, Z. Shao, Process investigation, electrochemical characterization and optimization of LiFePO₄/C composite from mechanical activation using sucrose as carbon source, *Electrochim. Acta* 54 (2009) 2861–2868.
- [33] M. Lengyel, D. Elhassid, G. Atlas, W.T. Moller, R.L. Axelbaum, Development of a scalable spray pyrolysis process for the production of non-hollow battery materials, *J. Power Sources* 266 (2014) 175–178.
- [34] P.L. de Andres, R. Ramirez, J.A. Vergés, Strong covalent bonding between two graphene layers, *Phys. Rev. B* 77 (2008) 045403.
- [35] J.U. Lee, W. Lee, J.W. Yi, S.S. Yoon, S.B. Lee, B.M. Jung, B.S. Kim, J.H. Byun, Preparation of highly stacked graphene papers via site-selective functionalization of graphene oxide, *J. Mater. Chem. A* 1 (2013) 12893–12899.
- [36] K. Suenaga, M. Koshino, Atom-by-atom spectroscopy at graphene edge, *Nature* 468 (2010) 1088–1090.
- [37] C.W. Dannatt, H.J.T. Ellingham, Roasting and reduction processes. Roasting and reduction processes—a general survey, *Discuss. Faraday Soc.* 4 (1948) 126–139.
- [38] X.K. Huang, S.M. Cui, J.B. Chang, P.B. Hallac, C.R. Fell, Y.T. Luo, B. Metz, J.W. Jiang, P.T. Hurley, J.H. Chen, A hierarchical tin/carbon composite as an anode for lithium-ion batteries with a long cycle life, *Angew. Chem. Int. Ed.* 54

- (2015) 1490–1493.
- [39] M. Winter, J.O. Besenhard, Electrochemical lithiation of tin and tin-based intermetallics and composites, *Electrochim. Acta* 45 (1999) 31–50.
 - [40] J. Kaspar, C. Terzioglu, E. Ionescu, M. Graczyk-Zajac, S. Hapis, H.J. Kleebe, R. Riedel, Stable SiOC/Sn nanocomposite anodes for lithium-ion batteries with outstanding cycling stability, *Adv. Funct. Mater.* 24 (2014) 4097–4104.
 - [41] W. Ni, J.L. Cheng, L.Y. Shi, X.D. Li, B. Wang, Q. Guan, L. Huang, G.F. Gu, H. Li, Integration of Sn/C yolk-shell nanostructures into free-standing conductive networks as hierarchical composite 3d electrodes and the Li-ion insertion/extraction properties in a gel-type lithium-ion battery thereof, *J. Mater. Chem. A* 2 (2014) 19122–19130.
 - [42] F.S. Ke, L. Huang, L. Jamison, L.J. Xue, G.Z. Wei, J.T. Li, X.D. Zhou, S.G. Sun, Nanoscale tin-based intermetallic electrodes encapsulated in microporous copper substrate as the negative electrode with a high rate capacity and a long cycleability for lithium-ion batteries, *Nano Energy* 2 (2013) 595–603.
 - [43] Z.Q. Zhu, S.W. Wang, J. Du, Q. Jin, T.R. Zhang, F.Y. Cheng, J. Chen, Ultrasmall Sn nanoparticles embedded in nitrogen-doped porous carbon as high-performance anode for lithium-ion batteries, *Nano Lett.* 14 (2014) 153–157.
 - [44] Y. Yan, L.B. Ben, Y.J. Zhan, X.J. Huang, Nano-Sn embedded in expanded graphite as anode for lithium ion batteries with improved low temperature electrochemical performance, *Electrochim. Acta* 187 (2016) 186–192.
 - [45] Y.H. Xu, Y.J. Zhu, Y.H. Liu, C.S. Wang, Electrochemical performance of porous carbon/tin composite anodes for sodium-ion and lithium-ion batteries, *Adv. Energy Mater.* 3 (2013) 128–133.
 - [46] F.X. Xin, X.L. Wang, J.M. Bai, W. Wen, H.J. Tian, C.S. Wang, W.Q. Han, A lithiation/delithiation mechanism of monodispersed MSn_5 ($M = \text{Fe}, \text{Co}$ and FeCo) nanospheres, *J. Mater. Chem. A* 3 (2015) 7170–7178.
 - [47] B. Wang, B. Luo, X.L. Li, L.J. Zhi, The dimensionality of Sn anodes in Li-ion batteries, *Mater. Today* 15 (2012) 544–552.
 - [48] H.L. Zhu, Z. Jia, Y.C. Chen, N. Weadock, J.Y. Wan, O. Vaaland, X.G. Han, T. Li, L.B. Hu, Tin anode for sodium-ion batteries using natural wood fiber as a mechanical buffer and electrolyte reservoir, *Nano Lett.* 13 (2013) 3093–3100.
 - [49] J. Liu, P. Kopold, C. Wu, P.A. van Aken, J. Maier, Y. Yu, Uniform yolk-shell $\text{Sn}_4\text{P}_3@C$ nanospheres as high-capacity and cycle-stable anode materials for sodium-ion batteries, *Energy Environ. Sci.* 8 (2015) 3531–3538.
 - [50] W. Chen, D. Deng, Carbonized common filter paper decorated with Sn@C nanospheres as additive-free electrodes for sodium-ion batteries, *Carbon* 87 (2015) 70–77.
 - [51] Y.C. Liu, N. Zhang, L.F. Jiao, Z.L. Tao, J. Chen, Ultrasmall Sn nanoparticles embedded in carbon as high-performance anode for sodium-ion batteries, *Adv. Funct. Mater.* 25 (2015) 214–220.
 - [52] Y.H. Liu, Y.H. Xu, Y.J. Zhu, J.N. Culver, C.A. Lundgren, K. Xu, C.S. Wang, Tin-coated viral nanoforests as sodium-ion battery anodes, *ACS Nano* 7 (2013) 3627–3634.